Crystal and magnetic structure of the La$_{1-x}$Ca$_x$MnO$_3$ compound ($0.11 \leqslant x \leqslant 0.175$)

M. Pissas,[1,*] I. Margiolaki,[2] G. Papavassiliou,[1] D. Stamopoulos,[1] and D. Argyriou[3]

[1]*Institute of Materials Science, National Center for Scientific Research, Demokritos, 15310 Ag. Paraskevi, Athens, Greece*
[2]*European Synchrotron Radiation Facility (ESRF), Pluo 30.1.08 6 Rue J. Horowitz, 38043 Grenoble, Cedex 9, France*
[3]*Berlin Neutron Scattering Center, Hahn-Meitner-Institut, Glienicker Str. 100 D-14109, Berlin, Germany*

We studied the crystal and magnetic structure of the La$_{1-x}$Ca$_x$MnO$_3$ compound for ($0.11 \leqslant x \leqslant 0.175$) using stoichiometric samples. For $x < 0.13$ the system's ground state is insulating canted antiferromagnetic. For $0.13 \leqslant x \leqslant 0.175$ below the Jahn-Teller transition temperature (T_{JT}) the crystal structure undergoes a monoclinic distortion. The crystal structure can be described with $P2_1/c$ space group which permits two Mn sites. The unit-cell strain parameter $s = 2(a-c)/(a+c)$ increases for $T < T_{JT}$, taking the maximum value at the Curie point, and then decreases. Below $T_{M'M''} \approx 60$ K s abruptly changes slope and finally approaches $T=0$ K with nearly zero slope. The change of s at $T_{M'M''}$ is connected to a characteristic feature in the magnetic measurements. As x increases towards the ferromagnetic metallic boundary, although s is reduced appreciably, the monoclinic structure is preserved. The monoclinic structure is discussed with relation to the orbital ordering, which can produce the ferromagnetic insulating ground state. We also studied samples that were prepared in air atmosphere. This category of samples shows ferromagnetic insulating behavior without following the particular variation of the s parameter. The crystal structure of these samples is related to the so-called O^* ($c > a > b/\sqrt{2}$) structure.

I. INTRODUCTION

The nature of the ferromagnetic insulating state (FMI) in lightly doped La$_{1-x}$A$_x$MnO$_3$ (A=Sr, Ca, x=0.1–0.2) rare-earth manganite perovskites continues to offer significant challenges in our understanding of the physical properties of these materials. Typically, insulating compounds of this category are antiferromagnetic, and ferromagnetism is associated with a metallic behavior that arises from doping and double exchange. The FMI state can be realized with a certain orbital ordering favorable for ferromagnetism.[1] In the intermediate doping levels (x=0.23–0.4) where the ferromagnetic metallic (FMM) state is observed the double-exchange mechanism is able to explain some of the experimental results. Despite the numerous studies concerning the FMI phase of La$_{1-x}$Sr$_x$MnO$_3$ compound, for the Ca case only a few exist. Furthermore, the tendency of this system in particular to produce cation deficient samples complicates the situation. For the Sr case the x=0.125 sample shows a transition to a FMM state from paramagnetic insulating state, followed by an abrupt first-order transition to the FMI phase. The FMI state coexists with a weak antiferromagnetic component with the A-type magnetic structure as was found in LaMnO$_3$.[2] In addition, in some other studies[3,4] charge or orbital ordering have been proposed to occur in the FMI state.

The manganite perovskites of interest to this work consist of a three-dimensional (3D) network of corner-sharing BX_6 octahedra located at the nodes of a simple cubic lattice. At the center of the unit cell there is room for the A cation which will fit perfectly if $d_{A-X} = d_{B-X}\sqrt{2}$. When $d_{A-X} < d_{B-X}\sqrt{2}$ the BX_6 octahedra are tilted to fill the extra interstitial space (steric effect). The steric effect in La$_{1-x}$Ca$_x$MnO$_3$ compound leads to a lower symmetry structure with space group $Pnma$ (in comparison to the aristotype cubic perov-

skite $Pm\bar{3}m$ structure) which according to the Glazer's classification[5] belongs to the $\alpha^-\beta^+\alpha^-$ tilt system (adopted by GdFeO$_3$ and CaTiO$_3$ perovskites). The adoption of the GdFeO$_3$ tilting scheme in La$_{1-x}$Ca$_x$MnO$_3$ is due to the small radius of the La and Ca, with respect to its surrounding cage. Thus, in order that the La ion can be accommodated in the structure, the MnO$_6$ octahedra tilt. Practically MnO$_6$ octahedra rotation is not rigid. Below a characteristic temperature the La$_{1-x}$Ca$_x$MnO$_3$ compound for $x < 0.23$ displays cooperative Jahn-Teller (JT) distortion arising from ordering of the e_g orbital of the Mn^{+3} ion. This structure is denoted as[6] O^l and the unit cell satisfies the inequality $a > c > b/\sqrt{2}$. For this phase, Mn^{+3} e_g orbitals are ordered like the undoped parent compound LaMnO$_3$.

Two mechanisms have been proposed to explain the orbital ordering in degenerated transition-metal orbital states. The first is related with lattice distortions[7] and the second is a direct generalization of the usual superexchange which in the case of orbital degeneracy is present.[8] The orbital ordering can be described by using the pseudospin-1/2 T_i operator in such a way so that the state $|T^z = \pm 1/2\rangle$ corresponds to the orbitals $|3z^2 - r^2\rangle$ and $|x^2 - y^2\rangle$, respectively. An arbitrary distortion can be described by linear superposition of the states $|T^z = \pm 1/2\rangle$, e.g., $|\theta\rangle = \cos(\theta/2)|1/2\rangle + \sin(\theta/2)|-1/2\rangle$, where θ is an angle in the (T^z, T^x) plane.

Finally, there is a third orthorhombic phase, O^* ($c > a > b\sqrt{2}$), related to orbital disordered manganites ($x > 0.23$). The O^* structure is pseudocubic with the Mn-O bond lengths almost equal, indicating that it lacks a clear static JT distortion. Both phases exhibit the orthorhombic $Pnma$ symmetry.

In this paper we present a synchrotron x-ray and neutron-diffraction study, using carefully prepared stoichiometric La$_{1-x}$Ca$_x$MnO$_3$ ($0.11 \leqslant x \leqslant 0.175$) samples in an effort to isolate the structural and magnetic features that characterize the

FMI state. Our diffraction results on stoichiometric samples shows that the crystal structure at FMI regime is monoclinic $P2_1/c$. The temperature variation of the unit-cell parameters is nonmonotonic, defining the T_{JT} and $T_{M'/M''}$ temperatures. In addition, this monoclinic crystal structure permits two Mn crystallographic sites. This crystal structure is different from that of the cation deficient samples and samples that belong in the ferromagnetic metallic regime.

II. EXPERIMENTAL DETAILS

La$_{1-x}$Ca$_x$MnO$_3$ samples ware prepared by thoroughly mixing high-purity stoichiometric amounts of CaCO$_3$, La$_2$O$_3$, and MnO$_2$. The mixed powders reacted in air up to 1400 °C for several days with intermediate grinding. Finally the samples were slowly cooled to 25 °C. These samples are cation deficient.[9–11] In order to produce stoichiometric samples additional annealing in He atmosphere was applied. More specifically, in the final preparation step the samples were heated under He flow up to 1100 °C for 48 h followed by rapid cooling to room temperature. It is important to stress here that in the doping range examined in this work the samples fired in air in all preparation steps are not stoichiometric. Although these samples are ferromagnetic and insulating for $x < 0.2$, they do not exhibit all the features of the stoichiometric samples, especially the cooperative Jahn-Teller (JT) distortion feature for $T < T_{JT}$.

Neutron powder-diffraction (NPD) data were collected on the E6 and E9 neutron diffractometers at the Berlin Neutron Scattering Center (BENSC), located at the Hahn-Meitner-Institut, Berlin. The neutron powder-diffraction measurements on the E6 diffractometer were performed as a function of temperature at low angles using (002) reflection of pyrolytic graphite monochromator, giving a wavelength $\lambda = 2.4$ Å. For high-resolution crystal structure determinations we measured NPD data using the E9 diffractometer with a wavelength of $\lambda = 1.798$ Å [(511) reflection of a vertically bent Ge monochromator] and collimation $\alpha_1 = 18'$ (in pile collimator), $\alpha_2 = 20'$ (second collimator after monochromator), $\alpha_3 = 10'$ (third collimator after sample). The powdered samples were contained in a cylindrical vanadium can ($D = 8$ mm) mounted in an orange cryostat.

For high resolution x-ray-diffraction data we used the ID31 high-resolution powder-diffraction beamline of the European Synchrotron Radiation Facility (ESRF). For our measurements we select a wavelength $\lambda = 0.500\ 19$ Å. Nuclear and magnetic structures were determined and refined from the NPD data by using the Rietveld method with the FULLPROF suite of programs.[12] For synchrotron x-ray-diffraction data, the GSAS suite was used.[13,14] As peak shape function we used the Gaussians convoluted with axial divergence asymmetry function[15] for neutron data and the constant wavelength profile function no. 4 of the GSAS for the x-ray data. dc magnetization measurements were performed in a superconducting quantum interference device (SQUID) magnetometer (Quantum Design). Finally, for the ac susceptibility measurements we used a home-made ac susceptometer.
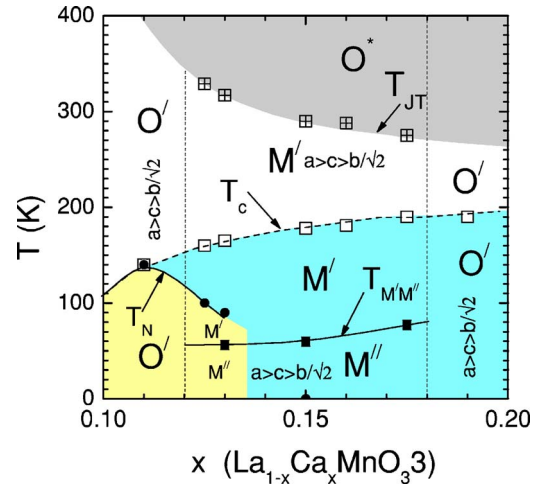

FIG. 1. (Color online) Ferromagnetic insulating part of the phase diagram of La$_{1-x}$Ca$_x$MnO$_3$ compound. The light yellow region corresponds to the CAF regime, and the light blue to the FMI regime. The symbols O*, O$'$, M$'$ and M$''$ have the following meaning: [O* orthorhombic *Pnma* symmetry with $c \geq a \geq b/\sqrt{2}$], [O$'$ orthorhombic *Pnma* symmetry with $a > c > b/\sqrt{2}$ and strong (intermediate) anisotropic bond lengths] and [M$'$,(M$''$) monoclinic $P2_1/c$ symmetry with $a > c > b/\sqrt{2}$ and strong (intermediate) anisotropic bond lengths]. The $T_{M'/M''}$ is defined at the temperature where the slope of the $a(T)$ and $b(T)$ curves change slope abruptly upon heating from $T = 0$. The T_{JT} curve is defined at the temperature where the $m(T)$ curves display a jumplike or slope-change behavior. The T_C and T_N are both estimated from neutron and magnetization data.

III. CRYSTAL STRUCTURE REFINEMENTS

Our structural and magnetization results on stoichiometric La$_{1-x}$Ca$_x$MnO$_3$, with an emphasis on the FMI regime, are summarized in Fig. 1 in the form of a phase diagram. The particular phase diagram is in good agreement with the one estimated by Biotteau *et al.*,[16] using single-crystal samples. The T_{JT} curve is defined at the temperature where the magnetization curves display a jumplike or slope-change behavior and the unit-cell parameter a (b) increases (decreases) abruptly on cooling. The particular behavior of the unit-cell constants resemble the situation observed in LaMnO$_3$ compound on cooling through the T_{JT} transition.[17] Depending on x, for $T < T_{JT}$ a symmetry change from *Pnma* to $P2_1/c$ occurs. The $T_C(x)$ and $T_N(x)$ lines concern the Curie and Néel temperatures as were estimated both from neutron and magnetization data. The line $T_{M'/M''}(x)$ is defined at the temperature where the $a(T)$ and $b(T)$ curves display an abrupt slope change, upon heating from $T = 0$. Based on the transition lines mentioned above the phase diagram of the La$_{1-x}$Ca$_x$MnO$_3$ compound depicted in Fig. 1 displays two distinct regions as the ground state is concerned. In the first region a canted antiferromagnetic (CAF) orthorhombic structure is present. In the second one, depending on x, ferromagnetic insulating (FMI) monoclinic and orthorhombic structures have been observed. The change from CAF to FMI ground states occurs in a narrow concentration regime $0.12 < x \lesssim 0.14$, where in neutron-diffraction patterns (*vide infra*)
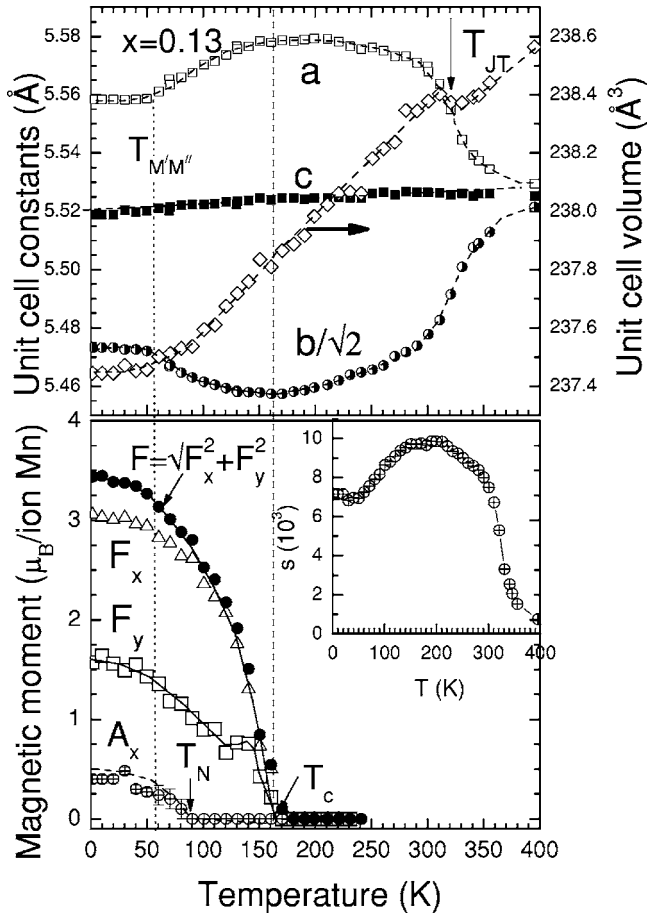
FIG. 2. Upper panel: temperature variation of the lattice parameters and unit-cell volume for $La_{0.87}Ca_{0.13}MnO_3$ compound. Lower panel: temperature variation of the ordered ferromagnetic and antiferromagnetic moments. The ferromagnetic components are denoted by F and the antiferromagnetic with A. The inset shows the temperature variation of the spontaneous orthorhombic strain [$s = 2(a-c)/a+c$]. Lines through the experimental points are guides to the eye.

a ferromagnetic transition (T_C) is observed first and after an antiferromagnetic transition (T_N) has been observed upon cooling. Our high-resolution synchrotron x-ray-diffraction patterns revealed that the true symmetry of the samples in the boundary of the CAF and FMI regimes and partially in the FMI regime is monoclinic with a very small monoclinic angle ($\gamma = 0.04° - 0.1°$). This regime is denoted by symbol M' in the phase diagram. The temperature variation of the unit cell parameters in the FMI regime revealed an additional structural transformation which occurs upon heating from $T = 0$ at temperature $T_{M'/M''}$. The magnitude of the unit cell changes at the $T_{M'/M''}$ reduces when the x is in the CAF-FMI(M) and FMI(M')-FMI(O') phase boundaries. In this phase diagram the ferromagnetic to paramagnetic (T_C), JT (T_{JT}), and $T_{M'/M''}$ transition lines are all estimated from neutron and magnetic measurements.

Figures 2–4 (upper panels) show the temperature variation of the unit-cell parameter for $x = 0.13$, 0.15, and 0.175 samples using the pseudo-orthorhombic description of the unit cell. For $T < T_{JT}$, the unit-cell parameters follow the in-
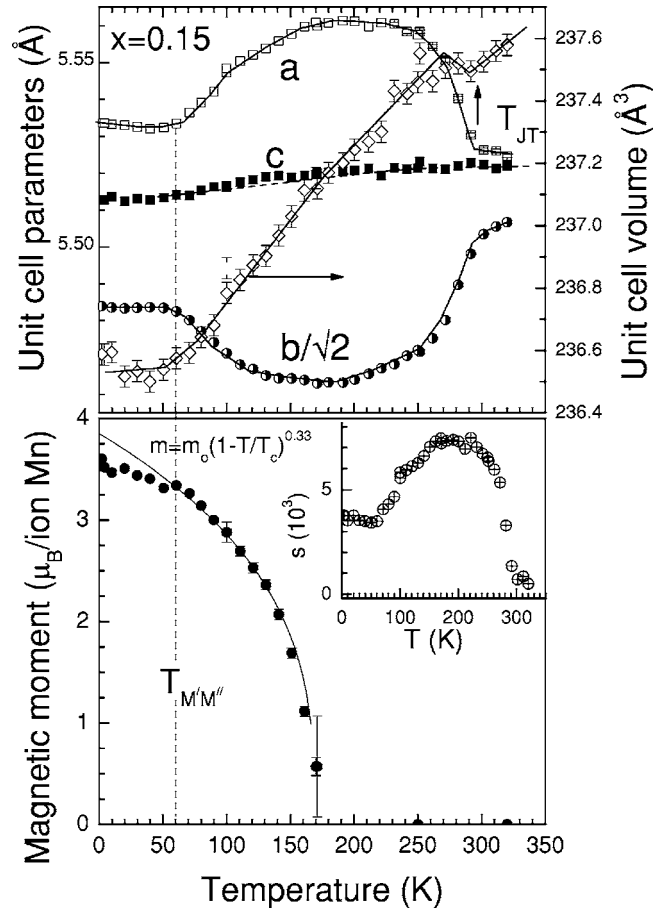
FIG. 3. Upper panel: temperature variation of the lattice parameters and unit-cell volume for $La_{0.85}Ca_{0.15}MnO_3$ compound. Lines through the experimental points are guides to the eye. Lower panel: temperature variation of the ordered ferromagnetic moment. The solid line is the calculated ordered moment supposing a power law. The inset shows the temperature variation of the spontaneous orthorhombic strain [$s = 2(a-c)/a+c$].

equality $a > c > b/\sqrt{2}$, a fact implying that in this pseudo-orthorhombic description the O' structure is realized in the whole temperature regime studied in this work. For all the samples there is a temperature region where the unit-cell parameters change abruptly (a increases, $b/\sqrt{2}$ decreases, and c decreases slightly) resembling the situation observed[17] in the $LaMnO_3$ compound due to the orbital ordering state. As it is mentioned above, we define the transition temperature T_{JT} as the point where an extreme in the da/dT curve occurs, in the high-temperature regime of the data. This particular assignment agrees with the magnetic measurements (*vide infra*). The orthorhombic strain parameter $s = 2(a-c)/(a+c)$ (see Figs. 2–4, lower panels) becomes maximum at the ferromagnetic transition temperature. Furthermore, for $T < T_c$ s decreases during cooling and finally for $T < T_{M'/M''} \sim 60$ K (for the $x = 0.13$ sample) it becomes almost temperature independent. The particular behavior reveals that the FMI state does not concern only the spin degrees of freedom but is also related with the lattice and orbital ones. The temperature variation of the unit-cell volume $V(T)$ exhibits a discontinuous change at T_{JT} implying that the JT
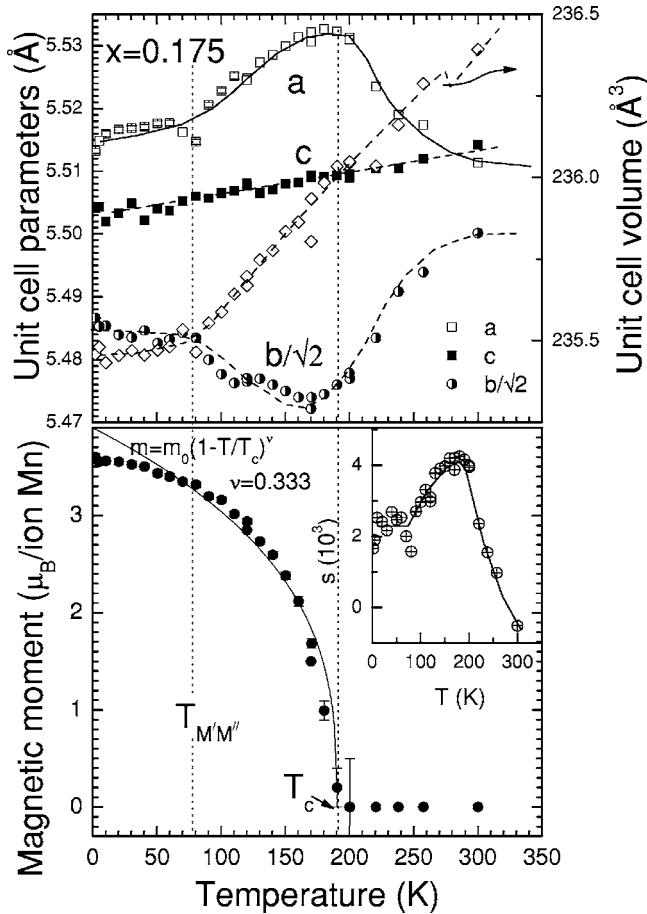
FIG. 4. Upper panel: temperature variation of the lattice parameters and unit-cell volume for $La_{0.825}Ca_{0.175}MnO_3$ compound. Lines through the experimental points are guides to the eye. Lower panel: temperature variation of the ordered ferromagnetic moment. The solid line is the calculated ordered moment supposing a power law. The inset shows the temperature variation of the spontaneous orthorhombic strain $[s=2(a-c)/a+c]$.

distortion is first order. As x increases the volume jump is difficult to be identified, on the basis of the available diffractometer resolution. It is very likely that the JT structural transition becomes second order for $x \geqslant 0.175$. Above and below T_{JT} the unit-cell volume decreases with temperature nearly linearly, showing a small slope change at T_C. Finally, at $T_{M'M''}V(T)$ displays a pronounced slope change for all samples.

Let us present now the high-resolution synchrotron x-ray data. The samples for $0.125 \leqslant x \leqslant 0.175$ for $T < T_{JT}$ exhibited additional reflections that cannot be accounted for the *Pnma* space group. More specifically, we observed splitting of the $(hk0)$, and (hkl) diffraction peaks not allowed in the *Pnma* space group. This splitting is compatible with the $P112_1/a \equiv P2_1/c$ (no 14, unique *c* axis) space group. Figure 5 depicts the high-resolution synchrotron x-ray-diffraction data for the $La_{0.85}Ca_{0.15}MnO_3$ sample at $T=5$ K, as an example. One can see very clearly the splitting of the diffraction peaks with nonzero *h* and *k*. We obtained similar data also for the other samples $x=0.125-0.175$. In this monoclinic distortion a glide-plane element is preserved, while the n and m elements

are lost. The loss of the mirror plane may be signaling a change of the JT order from *C*-type orbital ordering (that is followed by $LaMnO_3$) to a new one. We note that similar monoclinic distortions have been detected in $La_{1-x}Sr_xMnO_3$ ($x=0.11-0.5$) compounds.[18] Based on this critical information about the symmetry of the structure we refine the neutron data using the $P2_1/c$ space group. The mirror plane at $y=1/4$ being present for the *Pnma* space group is now absent, resulting in two Mn sites along the *b* axis, the first at $(1/2,0,0)$ and the second at $(1/2,1/2,0)$. Similarly, instead of one plane oxygen site (O2, *Pnma* symmetry) there are two now in the $P2_1/c$ symmetry. Thus in this new symmetry two crystallographically independent Mn sites produce a layer-type arrangement of two different MnO_6 octahedra along the *b* axis. The refinement strategy employed in this work was to first optimize the scale factor, background, unit-cell parameters, and zero-shift errors. Subsequently, we refined the atomic positional and isotropic thermal parameters. In order to reduce the number of parameters we decided to refine the thermal parameters for all the sites isotropically and we kept equal the thermal parameters of the Mn and O2 sites. Figures 6 and 7 show two representative Rietveld plots of neutron data for the $La_{0.85}Ca_{0.15}MnO_3$ sample at 320 and 2 K, respectively. The corresponding structural parameters for all the studied samples are reported in Tables I–III.

Figure 8 shows projections of the monoclinic structure of the $La_{0.85}Ca_{0.15}MnO_3$ compound for $T=170$ K on the *bc* and *ab* planes, respectively. All the samples show qualitatively the same behavior, as far as the variation of the structural parameters with temperature is concerned. Nevertheless, there are significant quantitative differences related to the influence of the hole doping through Ca substitution.

The Bragg peaks are quite sharp for $T > T_{JT}(x)$ but for $T < T_{JT}(x)$ they develop a pronounced selective peak broadening. In order to account for the selective peak broadening the Stephens[19] microstrain model was used. As our Rietveld refinement results reveal the microstrain parameters follow the temperature variation of the unit-cell parameters. The most significant broadening is related to S_{202} and S_{400} parameters. The S_{202} strain parameter describes a correlated-type random strain between *a* and *c* crystallographic directions and it is reasonable to be attributed to some kind of local static orbital ordering correlations. The average structure revealed a cooperative JT distortion which increases as temperature decreases. Parallel to this behavior, there is an antagonistic interaction which produces correlated fluctuation of the cell constants. These fluctuations are directly connected with the development of the ferromagnetic long-range order and temperature variation of the unit-cell parameters. The microstrain parameters take the maximum value at T_C. Most importantly the microstrain parameters are reduced about 30% at $T_{M'M''}$ and below this temperature remain nearly temperature independent. Consequently, our structural data reveal a complex magnetoelastic behavior for $T < T_C$, that characterizes the FMI regime of the $La_{1-x}Ca_xMnO_3$ compound.

Anisotropic broadening is usually connected with the presence of correlated structural defects, due to the preparation method, or is inherent to structural or magnetic transfor-
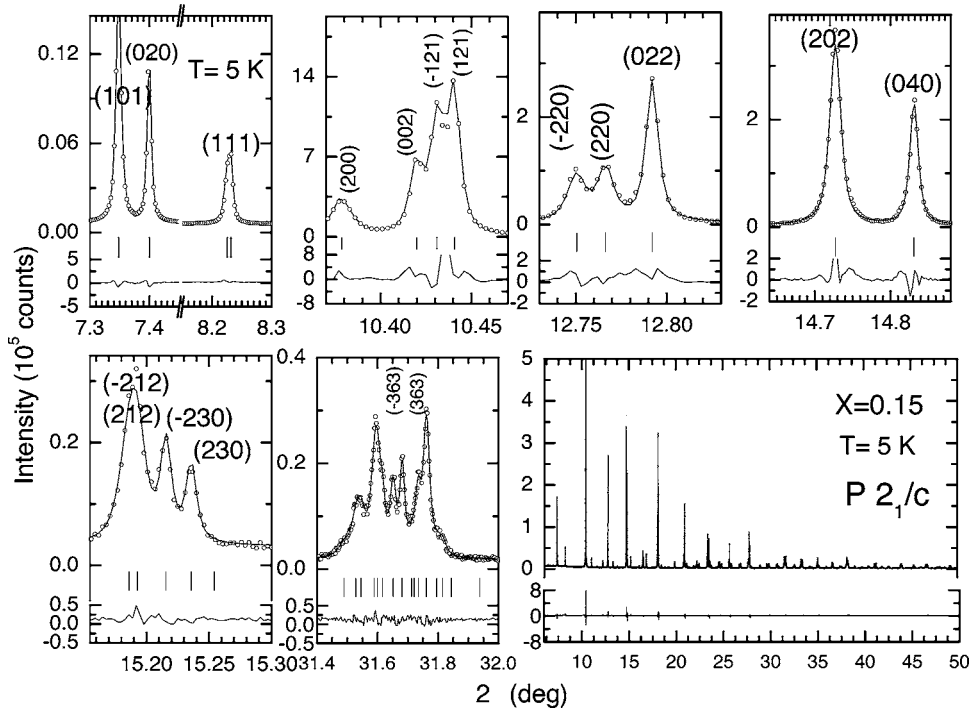
FIG. 5. Rietveld plot for $La_{0.85}Ca_{0.15}MnO_3$ at $T=5$ K using the high-resolution x-ray-diffraction data from ID31 beam line of the ESRF. Shown are details of the diffraction peaks where the characteristic peak splitting compatible with $P2_1/c$ space group is expected.

mations. Since we observe temperature dependence in the microstrain parameters, the case of the structural defects caused by the preparation method should be ruled out, because in this case a temperature-independent behavior is expected. It is natural to ask what is the physical origin of the particular temperature variation of the microstrain parameters. Essentially, the anisotropic peak broadening concerns the lattice planes $(h00)$ and $(h0l)$, meaning that there is some modulation along the a axis and $\mathbf{a}+\mathbf{c}$ direction. Our findings may be related with recent theoretical studies where the important role of the elastic energies (strain) in determining the ground state of the system has been pointed out.[20,21] Furthermore, the anisotropic broadening may originate from grains which contain different structural twin domains corroborated by the successive magnetostructural transformation occurring upon cooling. Finally, one cannot disregard the case where phase separation is present especially near the CAF-FMI phase boundary. In such a case several phases with nearly similar parameters occur producing indirectly a selective peak broadening, which is accounted for by microstrain formalism.

IV. BOND LENGTHS

In Fig. 9 are depicted the temperature variation of the Mn-O bond lengths for $x=0.125$, 0.15, and 0.175 samples, deduced from neutron-diffraction data. For $T<T_{JT}$ the crystal structure of the $La_{1-x}Ca_xMnO_3$ in the FMI regime based on the $P2_1/c$ space group have two Mn sites. As the Ca content increases the long Mn2-O bond length (which has been attributed to the d_{z^2} orbital) decreases. The short Mn2-O bonds are approximately at the same level as in the $LaMnO_3$ case. Concerning the intermediate Mn2-O bond, its magnitude is above the corresponding one of $LaMnO_3$. It is inter-

esting to note that the long and short bonds follow the temperature variation of the a and c cell parameters or in other words these bonds define the temperature variation of the unit-cell parameters. Based on the similarities of the Mn2-O bond lengths with those of $LaMnO_3$, it is reasonable to attribute the Mn2 site to a Mn^{+3}-like site in the $La_{1-x}Ca_xMnO_3$ ($0.125 \leqslant x \leqslant 0.175$) compound.

Let us turn now to the Mn1-O bond lengths. As their magnitude is concerned these bonds are more close to the bond lengths of MnO, observed in the FMM region of the phase diagram. In Fig. 9 (upper panel) with bold lines, the Mn-O bond lengths observed in the $La_{0.75}Ca_{0.25}MnO_3$ compound are depicted. One can see that as x increases the Mn1-O bond lengths approach these lines. It is plausible to attribute the Mn1 site to a mixed-valence Mn-like site as observed in the $La_{0.75}Ca_{25}MnO_3$ compound. As x reduces towards the CAF regime the Mn1-O bond lengths become nondegenerated and move away from those of $La_{0.75}Ca_{0.25}MnO_3$ compound.[22]

Except for the metrical variation of the bond lengths there is an orientation difference, concerning the short Mni-O bonds ($i=1,2$) between the two Mn sites. In the Mn2 site (which resembles the $LaMnO_3$ case) the short bond lies in the ac plane, contrary to the Mn1 site, where the short Mn1O bond is directed, approximately, along the b axis. According to the authors' opinion this is the key point to which one can be based in order to explain the FMI phase. It is important to note the fundamental difference between the conventional JT orthorhombic O' and the monoclinic M' structures. The latter cannot be the usual C-type antiferrodistortive arrangement found in the O' structure in the $LaMnO_3$ and CAF part of the phase diagram. As proposed by Cox $et\ al.$[18] in the case of $La_{1-x}Sr_xMnO_3$, the loss of the mirror plane would be consistent with a change in JT order from C type to G type at which there is antiferrodistortive coupling of MnO_6 octahe-
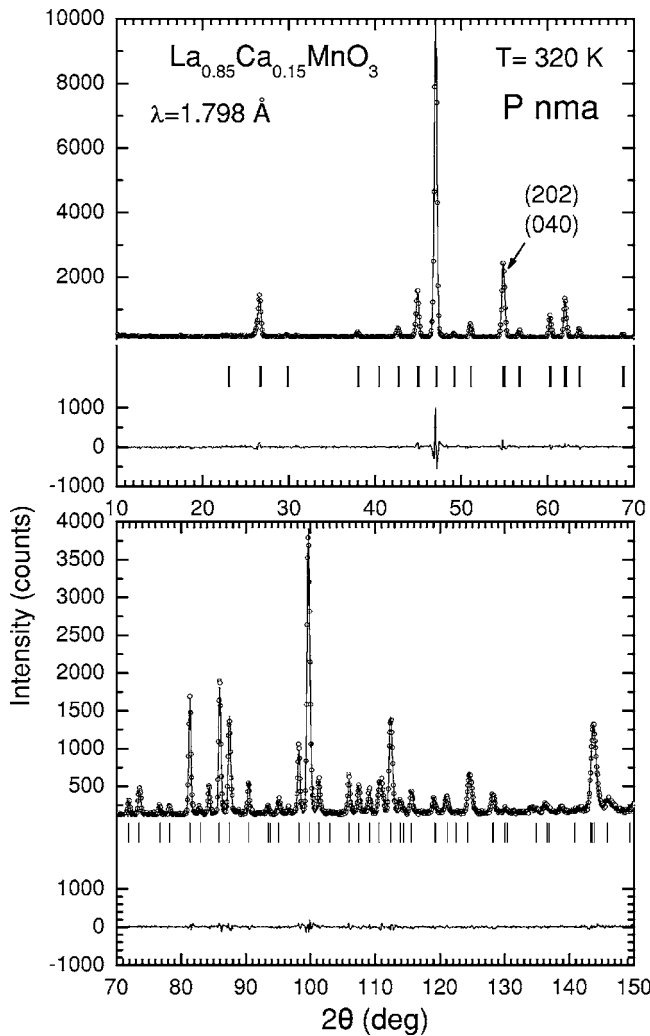
FIG. 6. Rietveld plot for $La_{0.85}Ca_{0.15}MnO_3$ at $T=320$ K. The observed data points are indicated by open circles, while the calculated and difference patterns are shown by solid lines. The positions of the reflections are indicated by vertical lines below the patterns.

FIG. 7. Rietveld plot for $La_{0.85}Ca_{0.15}MnO_3$ at $T=2$ K. The observed data points are indicated by open circles, while the calculated and difference patterns are shown by solid lines. The positions of the reflections are indicated by vertical lines below the patterns.

dra along the *b* direction instead of parallel coupling (see Fig. 8).

V. MAGNETIC MEASUREMENTS AND MAGNETIC STRUCTURE

Figures 10 and 11 (upper panels) show the temperature variation of the magnetic moment per Mn ion for the samples $x=0.15$ and 0.175, respectively, for several dc magnetic fields. We obtained similar magnetic measurement data also for $x=0.125$, 0.13, and 0.14 samples. In the lower panels of Figs. 10 and 11 we plot the temperature dependence of the normalized real part of the ac susceptibility, and the low-field dc magnetic moment (left axis). In addition, we plot the temperature variation of the inverse dc susceptibility (H/m) (right axis) measured under a dc field $H=5$ kOe. The abrupt increasing of the magnetic signal in the dc and ac measurements at $T_C=168$ K and $T_C=187$ K for $x=0.15$ and $x=0.175$, respectively, marks a transition from a paramagnetic
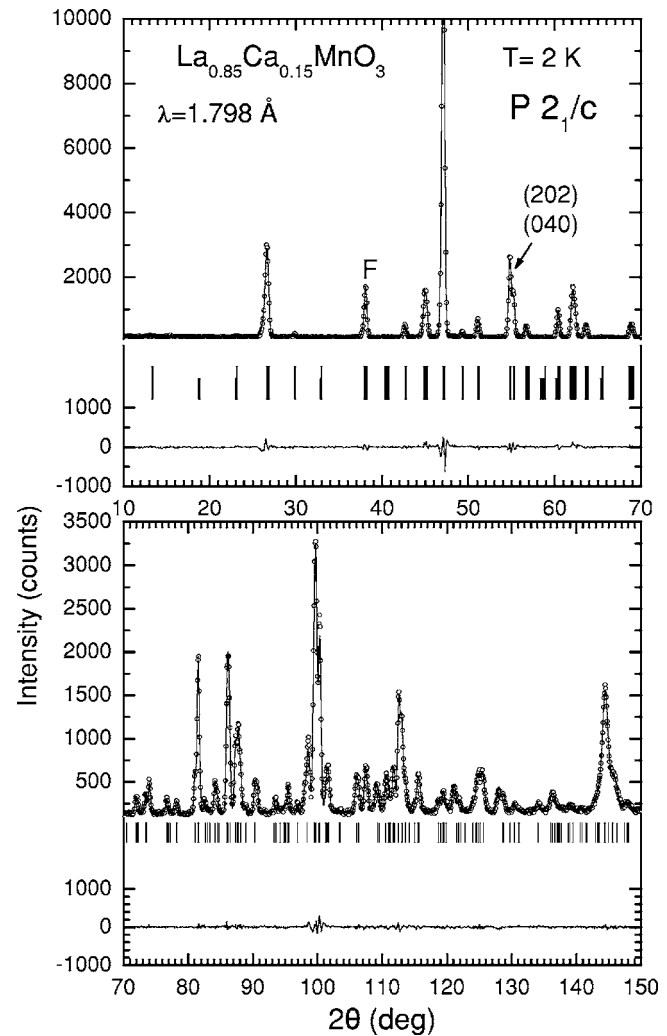
to ferromagnetic state, in agreement with neutron data (*vide infra*). The sharp peak at T_C in the χ' is related with the Hopkison effect, as we discussed in Ref. 9. Upon heating from $T=0$, $\chi'(T)$ slightly increases up to $T \approx T_{M'M''}$. For $T > T_{M'M''}$ $\chi'(T)$ increases in a stepwise fashion as the dashed vertical lines in Figs. 10 and 11 show. This peculiarity reveals the magnetic signature of the structural change that occurs at $T_{M'M''}$. The particular anomaly is present and in the dc magnetization measurements as it is seen, for example, in the upper panel of Fig. 10 where a steplike slope change occurs at $T_{M'M''}$.

Furthermore, a close inspection of the $m(T)$ curves at the paramagnetic regime reveals an additional anomaly which is related with JT distortion observed in the crystal structure data (see the inset of Fig. 10). This anomaly is more pronounced for the $x=0.11$ sample; its signature reduces as x increases and finally becomes hard to discern for the samples with $x \geq 0.175$. The anomaly in the magnetic measurements at T_{JT} is seen more clearly in the inverse susceptibility data (see lower panels of Figs. 10 and 11). Comparing these data

TABLE I. $La_{1-x}Ca_xMnO_3$ ($x=0.125$) structural parameters at several temperatures, as determined from Rietveld refinements based on neutron powder-diffraction data of the E9 diffractometer ($\lambda=1.797\,84$ Å). The monoclinic space group $P2_1/c \equiv P\,1\,1\,2_1/a$ (no. 14, unique c axis) was used. In this space group La, Ca O1, O2A, and O2B occupy the general $4e$ position (x,yz). Mn1 and Mn2 occupy the $2c(1/2,0,0)$ and $2d(1/2,1/2,0)$ positions, respectively. Numbers in parentheses are statistical errors of the last significant digit.

T (K)		300	198.4	121	48	2
a (Å)		5.5754(1)	5.5855(1)	5.5829(1)	5.5709(1)	5.5697(1)
b (Å)		7.7423(1)	7.7213(1)	7.7186(1)	7.7288(1)	7.7296(1)
c (Å)		5.5269(1)	5.5253(1)	5.5234(1)	5.5206(1)	5.5205(1)
γ (deg.)		90.125(3)	90.130(5)	90.127(4)	90.106(6)	90.107(5)
La, Ca	x	0.0319(4)	0.0344(3)	0.0348(6)	0.0342(3)	0.0341(3)
	y	0.2501(8)	0.2487(5)	0.2477(7)	0.2479(9)	0.2485(8)
	z	0.0058(5)	0.0049(4)	0.0055(4)	0.0064(4)	0.0061(4)
	B	0.69(4)	0.57(3)	0.43(3)	0.33(3)	0.37(3)
Mn1	B	0.38(7)	0.30(6)	0.24(6)	0.19(5)	0.17(6)
Mn2	B	0.38(7)	0.30(6)	0.24(6)	0.19(5)	0.17(6)
O1	x	0.4909(6)	0.4898(5)	0.4906(5)	0.4909(5)	0.4901(5)
	y	0.244(1)	0.247(1)	0.246(1)	0.248(1)	0.247(1)
	z	−0.0670(6)	−0.0679(4)	−0.0688(5)	−0.0687(4)	−0.0683(5)
	B	1.01(6)	0.87(5)	0.74(5)	0.60(4)	0.62(5)
O2A	x	0.213(1)	0.211(1)	0.209(1)	0.215(1)	0.223(1)
	y	−0.0380(9)	−0.0377(8)	−0.0392(7)	−0.0376(8)	−0.0374(9)
	z	0.784(1)	0.784(1)	0.784(1)	0.788(1)	0.783(1)
	B	1.06(5)	0.83(4)	0.66(4)	0.76(4)	0.73(4)
O2B	x	−0.207(1)	−0.207(1)	−0.208(1)	−0.205(1)	−0.207(1)
	y	0.4656(9)	0.4640(7)	0.4655(7)	0.4644(8)	0.4641(8)
	z	−0.764(1)	−0.763(1)	−0.764(1)	−0.778(1)	−0.766(1)
	B	1.06(5)	0.83(3)	0.66(4)	0.76(4)	0.73(4)
	R_p	7.0	5.9	6.4	5.7	5.9
	R_{wp}	9.2	7.6	8.2	7.5	7.8
	R_B	6.2	5.3	5.6	4.7	4.8
Mn1-O1$\times 2$		1.928(9)	1.947(8)	1.942(8)	1.95(1)	1.948(1)
Mn1-O2A$\times 2$		2.013(7)	2.026(6)	2.035(6)	2.022(8)	2.014(7)
Mn1-O2A$\times 2$		1.994(8)	1.986(6)	1.981(7)	1.971(9)	1.987(7)
Mn2-O1$\times 2$		2.014(9)	1.986(8)	1.993(8)	1.98(1)	1.990(1)
Mn2-O2B$\times 2$		2.102(7)	2.111(6)	2.099(6)	2.082(8)	2.095(7)
Mn2-O2B$\times 2$		1.884(8)	1.881(6)	1.887(6)	1.911(9)	1.891(7)

one can clearly see that the jump of H/m at T_{JT} is transformed to a slope change as x increases. The particular change at T_{JT} for the $x>0.175$ samples may mark a change of JT transition from first to second order.

Above and below T_{JT}, χ^{-1} can be fitted by a straight line implying a Curie-Weiss law [$\chi^{-1}=(T-\Theta)/C$]. The Curie constant is given by $C=(N/V_c)g^2\mu_B^2 S(S+1)/3k_B$, where N is the number of magnetic ions inside the unit cell, V_c is the unit-cell volume, $g\approx 2$ ($S=J$, $L=0$) is the Landé factor, μ_B is the Bohr magneton, S is the spin of the ion, k_B is Boltzmann's constant, and Θ is the Weiss constant. Since χ^{-1} is

nearly parallel above and below T_{JT} it is reasonable to attribute this change to Θ. Therefore since $\Theta \propto J$ (where J is the exchange coupling) the abrupt change in the χ^{-1} may be related to a discontinuous change of J above and below T_{JT}. The O' phase has larger exchange constants in comparison to the M' one. The intersection of H/m with the temperature axis, for $T<T_{JT}$ gives a $\Theta=175$ K, in good agreement with the Curie temperature estimated from neutron data (*vide infra*). From the Curie constant we estimate an effective magnetic moment per ion which is $6.01\mu_B$. This value is in disagreement with the one theoretically expected for an

TABLE II. La$_{1-x}$Ca$_x$MnO$_3$ ($x=0.15$) structural parameters at several temperatures, as determined from Rietveld refinements based on neutron powder-diffraction data of the E9 diffractometer ($\lambda=1.797\,84$ Å). At $T=320$ K the space group *Pnma* (no. 62) was used. La, Ca, and apical oxygen (O1) occupy the $4c(x,1/4,z)$ site, Mn the $4b(0,0,1/2)$ site, and the plane oxygen (O2) the general $8d$ site. For other temperatures the monoclinic space group $P2_1/c \equiv P\,1\,1\,2_1/a$ (no. 14, unique c axis) was used. In this space group La, Ca O1, O2A, and O2B occupy the general $4e$ position (x,yz). Mn1 and Mn2 occupy the $2c(1/2,0,0)$ and $2d(1/2,1/2,0)$ positions, respectively. Numbers in parentheses are statistical errors of the last significant digit.

T (K)		320	250	170	100	2
a (Å)		5.5246(1)	5.5573(1)	5.5614(1)	5.5480(1)	5.5300
b (Å)		7.7877(1)	7.7387(1)	7.7266(1)	7.7386(1)	7.7508
c (Å)		5.5219(1)	5.5213(1)	5.5195(1)	5.5159(1)	5.5081
γ (deg.)		90	90.140(1)	90.134(2)	90.0965(1)	90.0752
La, Ca	x	0.0263(4)	0.0300(3)	0.0311(3)	0.0309(3)	0.0303(2)
	y	0.25	0.2489(5)	0.2501(7)	0.2493(6)	0.2454(6)
	z	−0.0083(5)	0.0060(4)	0.0060(4)	0.0058(4)	−0.0065(4)
	B	0.54(5)	0.40(3)	0.42(3)	0.12(2)	0.15(3)
Mn1	B	0.36(7)	0.25(5)	0.19(5)	0.19(5)	0.16(5)
Mn2	B		0.25(5)	0.19(5)	0.19(5)	0.16(5)
O1	x	0.4910(8)	0.4912(4)	0.4914(4)	0.4905(5)	0.4909(4)
	y	0.25	0.2450(8)	0.246(1)	0.2429(8)	0.259(1)
	z	0.0684(7)	−0.0668(4)	−0.0675(1)	−0.0693(4)	−0.0680(5)
	B	0.94(7)	0.69(4)	0.58(4)	0.45(4)	0.484(4)
O2A	x	0.2817(6)	0.2180(7)	0.2188(8)	0.2212(9)	0.2219(9)
	y	0.0353(3)	−0.0381(5)	−0.0364(7)	−0.0375(6)	−0.0384(6)
	z	0.7238(6)	0.721(1)	0.780(1)	0.780(1)	0.782(1)
	B	0.88(5)	0.63(3)	0.58(3)	0.40(3)	0.32(3)
O2B	x		−0.2075(8)	−0.2059(9)	−0.206(1)	−0.2085(0)
	y		0.4659(6)	0.4639(7)	0.4657(7)	0.4666(6)
	z		−0.766(1)	−0.768(1)	−0.768(1)	−0.768(1)
	B		0.63(3)	0.58(3)	0.40(3)	0.32(3)
	R_p	6.9	5.1	6.2	6.0	6.1
	R_{wp}	9.0	6.8	7.9	8.0	7.9
	R_B	4.3	4.1	5.6	3.7	3.6
Mn1-O1×2		1.9839(8)	1.932(6)	1.941(8)	1.919(6)	1.973(7)
Mn1-O2A×2		2.006(3)	1.999(5)	1.996(6)	1.986(6)	1.973(6)
Mn1-O2A×2		1.9634(3)	1.992(5)	1.991(6)	1.995(7)	2.002(7)
Mn2-O1×2			2.007(6)	1.994(8)	2.026(6)	1.975(7)
Mn2-O2B×2			2.092(5)	2.094(6)	2.086(6)	2.071(6)
Mn2-O2B×2			1.886(2)	1.893(6)	1.891(7)	1.893(6)

appropriate, random mixture of Mn^{+3} and Mn^{+4} ions, $\mu^2 = (1-x)g^2 S_3(S_3+1)+xg^2 S_4(S_4+1)$, where $S_{3,4}=2$ and 3/2 for Mn^{+3} and Mn^{+4}, respectively. An enhanced paramagnetic effective moment has also been observed in the Sr-based compound and has been attributed to magnetic clusters.[23,24] The larger effective magnetic moment of the M^l phase for $x>0.15$ may be related with the idea of the magnetic polaron that "survives" in the regime $T_C \leqslant T \leqslant T_{JT}$. We must note that this state is more relevant when the system moves away from

the CAF regime. Finally, it is interesting to note the similarity of our bulk magnetic moment data with those of Refs. 23 and 24 referring to the Sr compound. There is, however, a distinct difference below T_C. Our ac susceptibility, reduces significantly for $T<T_{M'M''}$, while in the Sr case it increases in a stepwise fashion. This "fine" difference may imply that the M'' states of Ca and Sr compounds are different. The orthorhombic strain and the long in-plane Mn-O2 distance reduction is very similar but the ordered magnetic moment,

TABLE III. $La_{1-x}Ca_xMnO_3$ ($x=0.175$) structural parameters at several temperatures, as determined from Rietveld refinements based on neutron powder-diffraction data of the E9 diffractometer ($\lambda = 1.79784$ Å). At $T=300$ K the space group *Pnma* (no. 62) was used. La, Ca, and apical oxygen (O1) occupy the $4c(x,1/4,z)$ site, Mn the $4b(0,0,1/2)$ site, and the plane oxygen (O2) the general 8d site. For other temperatures the monoclinic space group $P2_1/c \equiv P\ 1\ 1\ 2_1/a$ (no. 14, unique c axis) was used. In this space group La, Ca O1, O2A, and O2B occupy the general 4e position (x,yz). Mn1 and Mn2 occupy the $2c(1/2,0,0)$ and $2d(1/2,1/2,0)$ positions, respectively. Numbers in parentheses are statistical errors of the last significant digit.

T (K)		300	200	170	120	70	2
a (Å)		5.5113(1)	5.5275(1)	5.5323(1)	5.5242(1)	5.5165(1)	5.5152(1)
b (Å)		7.7778(1)	7.7449(2)	7.7414(1)	7.7453(1)	7.7553(1)	7.7568(1)
c (Å)		5.5142(1)	5.5114(1)	5.5104(1)	5.5080(1)	5.5050(1)	5.5042(1)
γ (deg.)	90.0		90.094(6)	90.09(1)	90.063(5)	90.059(4)	90.056(4)
La, Ca	x	0.0252(4)	0.0283(3)	0.0292(5)	0.0290(3)	0.0280(3)	0.0278(3)
	y	0.25	0.248(1)	0.244(1)	0.247(1)	0.249(1)	0.248(1)
	z	−0.008	0.0063(5)	0.0087(7)	0.0074(5)	0.0070(6)	0.0077(6)
	B	0.57(4)	0.44(3)	0.70(4)	0.37(3)	0.28(3)	0.28(3)
Mn1	B	0.37(7)	0.1(1)	0.34(8)	0.08(6)	0.11(6)	0.13(6)
Mn2	B		0.1(1)	0.34(8)	0.08(6)	0.11(6)	0.13(65)
O1	x	0.4927(8)	0.4914(6)	0.4910(8)	0.4927(6)	0.4913(6)	0.4913(5)
	y	0.25	0.247(1)	0.246(1)	0.248(1)	0.250(1)	0.251(1)
	z	0.0680(8)	−0.0669(5)	−0.0646(7)	−0.0671(5)	−0.0665(6)	−0.0673(3)
	B	0.86(7)	0.65(5)	0.77(6)	0.46(5)	0.38(5)	0.37(5)
O2A	x	0.2792(7)	0.221(1)	0.221(2)	0.224(1)	0.221(1)	0.221(1)
	y	0.0344(4)	−0.035(1)	−0.0360(9)	−0.0369(8)	−0.033(1)	−0.033(1)
	z	0.7240(7)	0.781(1)	0.771(2)	0.770(1)	0.781(1)	0.778(2)
	B	0.7224(7)	0.62(3)	1.04(5)	0.64(4)	0.50(3)	0.56(4)
O2A	x		−0.209(1)	−0.209(2)	−0.208(1)	−0.213(1)	−0.214(1)
	y		0.464(1)	0.4676(9)	0.4666(9)	0.462(1)	0.462(1)
	z		−0.766(1)	−0.771(2)	−0.780(1)	−0.770(1)	−0.774(2)
	B		0.62(4)	1.04(5)	0.64(4)	0.50(3)	0.56(4)
	R_p	6.0	5.4	6.8	5.8	6.1	6.2
	R_{wp}	8.0	7.0	9.4	7.6	8.0	8.0
	R_B	3.3	3.6	5.6	4.2	3.8	3.8
Mn1-O1×2		1.9809(1)	1.949(1)	1.93(1)	1.95(1)	1.979(1)	1.98(1)
Mn1-O2A×2		1.996(4)	1.973(8)	2.00(1)	2.000(8)	1.968(8)	1.980(9)
Mn1-O2A×2		1.973(4)	1.995(8)	1.95(1)	1.959(8)	1.989(9)	1.97(1)
Mn2-O1×2			1.993(1)	1.99(1)	1.98(1)	1.96(1)	1.96(1)
Mn2-O2B×2			2.074(8)	2.04(1)	2.029(8)	2.043(8)	2.028(9)
Mn3-O2B×2			1.891(8)	1.92(1)	1.944(9)	1.922(8)	1.93(1)

bulk magnetic moment, and ac susceptibility show opposite change at $T_{M/M''}$.

Let us present now the neutron-diffraction data related with the magnetic structure. The magnetic structures for all the samples are best monitored by observing the neutron-diffraction patterns, using data from the E6 instrument with $\lambda = 2.4$ Å. Figure 12 show portions of neutron-diffraction patterns in the region where the magnetic coherent intensity is maximum for the $x=0.11$ sample. Similar data were also collected for the other samples. In all samples we observed an increasing of the Bragg intensity for the peaks (101) and (020) for $T < T_C$, something which is compatible with the development of long-range ferromagnetic order. In addition, the samples $x=0.11$, 0.125, and 0.13 show the characteristic magnetic peaks of the A antiferromagnetic structure. The most pronounced magnetic Bragg peak of the A-magnetic structure is the (010) located at $\approx 18°$. As x increases, the area of this peak at $T=2$ K reduces, implying that the anti-

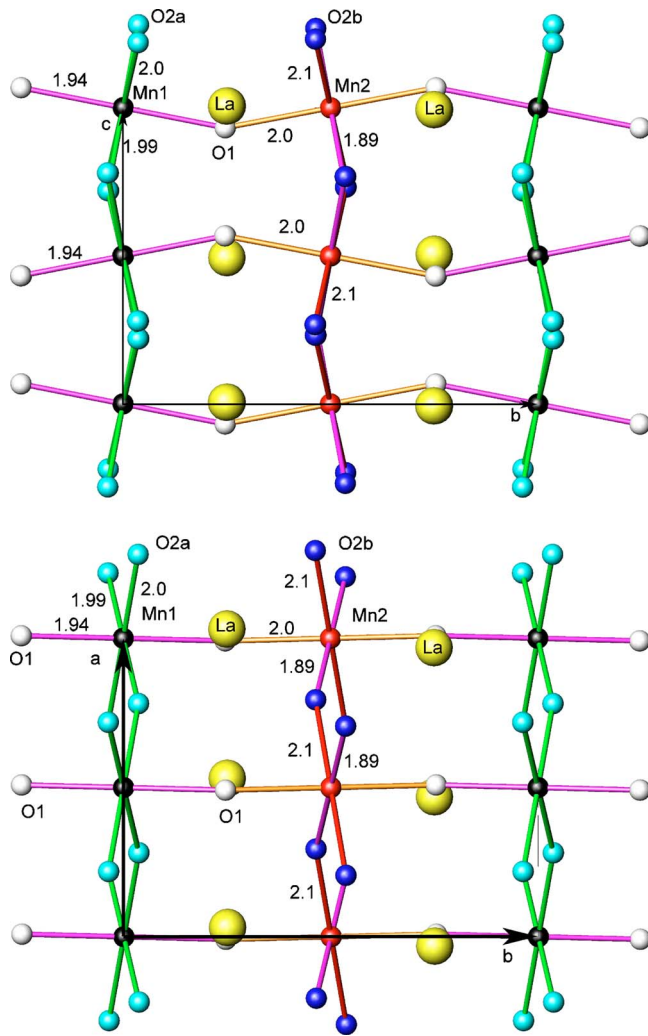FIG. 8. (Color online) Crystal structure of $La_{0.85}Ca_{0.15}MnO_3$ compound at $T=170$ K. The upper and lower panels show the projections along the a and c axis, respectively. The large hatched, small filled, and intermediate open spheres represent La, Mn, and O ions, respectively. The Mn1, Mn2 sites are located at $y=0$ and $y=1/2$ planes, respectively (b axis is the largest one). The sort Mn1-O, Mn2-O bonds denoted by grey rods are directed along and perpendicular to the b axis, respectively.
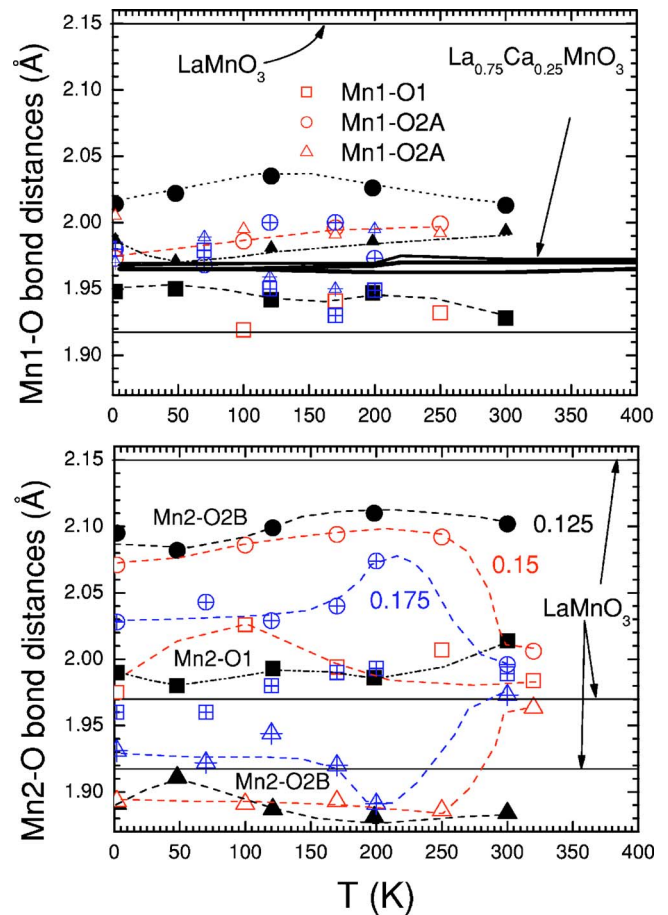

FIG. 9. (Color online) Mn-O_i ($i=1, 2$) bond distances as a function of temperature for $x=0.125$, 0.15, and 0.175 samples. The upper panel shows the Mn1-O bonds and lower panel the Mn2-O bonds (Mn1-O1, Mn2-O1 are the apical bonds and Mn1-O2A, Mn2-O2B are the in-plane bonds). Lines through the experimental points are guides to the eye. The solid, open and "crossed" symbols correspond to $x=0.125$, 0.15, and 0.175, respectively. The data for the LaMnO$_3$ (thin lines) and $La_{0.75}Ca_{0.25}MnO_3$ (thick lines) samples are also included for a direct comparison.

ferromagnetic ordered moment reduced and finally becomes zero for $x \gtrsim 0.14$. We refined the $x=0.11$ sample, where the pronounced orthorhombicity enables us to safely determine the spin components along the three axes. The lower panel of Fig. 12 shows a decomposition of the neutron-diffraction pattern at $T=2$ K, which consists of the patterns coming from the A-type antiferromagnetic, the ferromagnetic, and the crystal structure patterns. The inset of the lower panel of Fig. 12 shows the calculated patterns of models $F_x F_y A_z$ and $A_x F_y F_z$ (F_x denotes ferromagnetic moment along the x axis and A_x is the magnetic moment along the x axis which follows the A-antiferromagnetic structure). The agreement between the theoretical and experimental profile is better for the $A_x F_y F_z$ model. This magnetic model is closely connected with the canted magnetic structure observed in the LaMnO$_3$ compound.[25] Similarly, for the $x=0.125$ sample, except for

the major ferromagnetic component, small intensity coming from A-type antiferromagnetic structure is present. In addition, the negligible intensity of the (200) magnetic peak implies that the ferromagnetic component cannot have large components along the b or the c axis. Therefore there are two possibilities. The first is that the antiferromagnetic component is parallel with the c axis, while the ferromagnetic component is parallel with the a and b axes. The second possibility is that both the antiferromagnetic and part of the ferromagnetic component are parallel with a axis. Since it is not possible to have simultaneous ferromagnetic and antiferromagnetic spin components along the a axis in the same domain these two different magnetic states concern different domains. This finding is not strange since in this concentration regime the phase boundary separating the CAF and FMI ground states exists.

For the sample $x=0.15$ the NDP at $T=2$ K shows only ferromagnetic magnetic peaks. The orthorhombicity of the sample permits the calculation of the orientation of the mag-
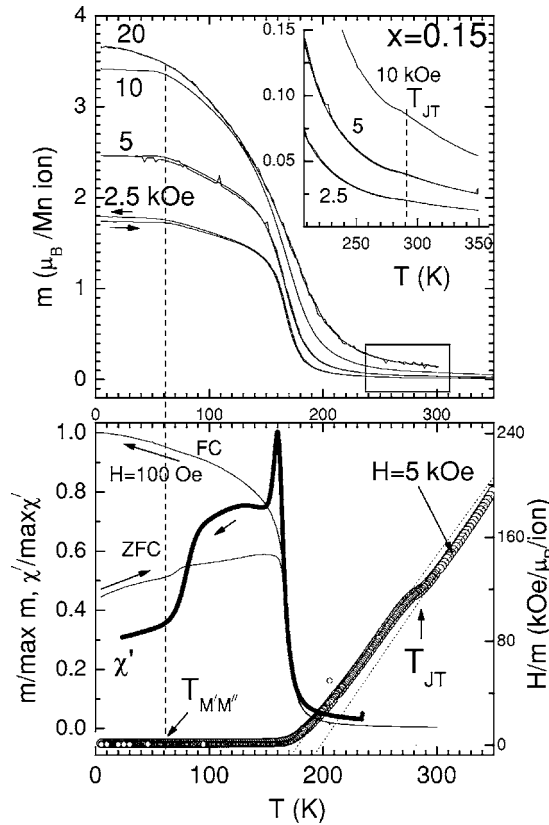
FIG. 10. Upper panel: temperature variation of the bulk magnetic moment per ion Mn for $La_{0.85}Ca_{0.15}MnO_3$. The data were collected under the indicated magnetic fields using the standard ZFC-FC procedure. The inset shows the details of the measurements at the T_{JT} region. Lower panel: temperature variation of the inverse dc magnetic moment, normalized real part of the fundamental ac-susceptibility (bold line) and normalized ZFC and FC bulk magnetic moment measured under a dc field 100 Oe (thin line). The dotted lines corresponds to the Curie-Weiss law used to fit the data above and below T_{JT}. The vertical dashed line indicates the $T_{M'/M''}$.

netic moment with respect to the crystallographic axes.[26] Thus the $\mathbf{m} \| b$ axis case should be excluded. If the magnetic moment was along the b axis the magnetic contribution at the (020) peak should be zero. Based on the best agreement between observed and theoretically calculated profiles we conclude that the ordered magnetic moment should lie on the ac plane with its larger component along the a axis. Nevertheless, a small component along the b axis cannot be totally excluded. The ordered magnetic moments as estimated from Rietveld refinements for the $x=0.13, 0.15,$ and 0.175 samples are plotted in the lower panels of Figs. 2–4, respectively. A weak but distinctive anomaly is present in the temperature variation curves of the ordered magnetic moments at $T_{M'/M''}$. It is imperative to note that for $T \approx T_{M'/M''}$ the ordered magnetic moment curve, for $x=0.15$ and 0.175 samples, displays a small slope change. For samples $x=0.11, 0.125,$ and 0.13 where we can detect the magnetic peak from the A-type magnetic structure, this anomalous behavior certainly is related with the antiferromagnetic component. For $x \gtrsim 0.15$ it is possible that a small percentage of the spin of Mn ions may prefer a glasslike behavior for $T < T_{M'/M''}$, as the ac suscepti-
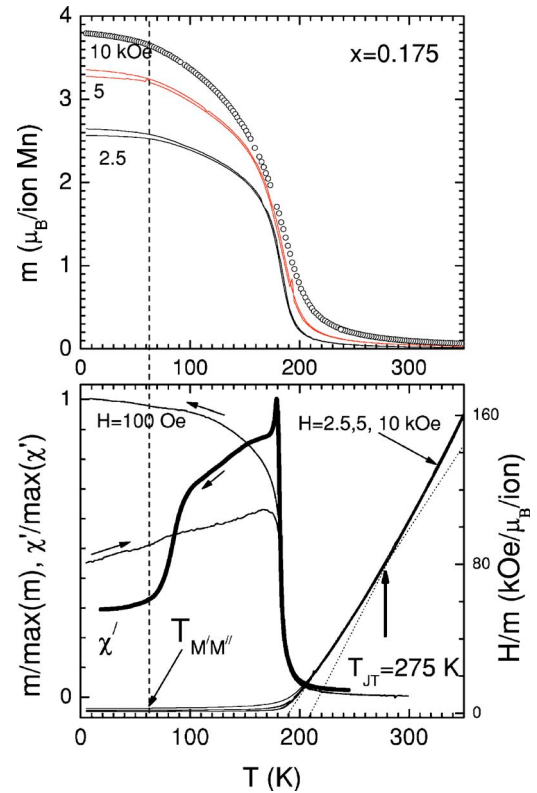
FIG. 11. (Color online) Upper panel: temperature variation of the bulk magnetic moment per ion Mn for $La_{0.825}Ca_{0.175}MnO_3$. The data were collected under the indicated magnetic fields using the standard ZFC-FC procedure. Lower panel: temperature variation of H/m, normalized real part of the fundamental ac susceptibility (bold line) and normalized ZFC and FC bulk magnetic moment measured under a dc magnetic field 100 Oe (thin line). The dotted lines correspond to the Curie-Weiss law used to fit the data above and below T_{JT}. The vertical dashed line indicates the $T_{M'/M''}$.

bility measurements show.[27] Concerning this "strange" magnetic component it is not clear how it is connected with the structural transition at the same temperature. One could invoke the idea of the phase separation to explain this behavior, however, the bulk character of the concomitant structural transition at $T_{M'/M''}$ is not so favorable for this interpretation. Based on the experimental data one may say that the structural transition prevents some part of the Mn spin to participate in the long-range ordering.[9,27] This structural transition should be related with the orbital degree of freedom in agreement with Mossbauer[28] and NMR (Ref. 29) data.

VI. DISCUSSION

Unexpectedly, the space group $P2_1/c$ has been used by Lobanov *et al.*[30] in order to describe the crystal structure for a sample with nominal stoichiometry $La_{0.85}Ca_{0.15}MnO_3$ prepared by liquid road and final reaction temperature 900 °C. However, although this space group is the same with that used in our study, several differences exist. More specifically: (a) The ac susceptibility and resistivity data are different. (b) The sample of Lobanov *et al.*[30] does not show the pseudo-orthorhombic splitting seen in our data and in the
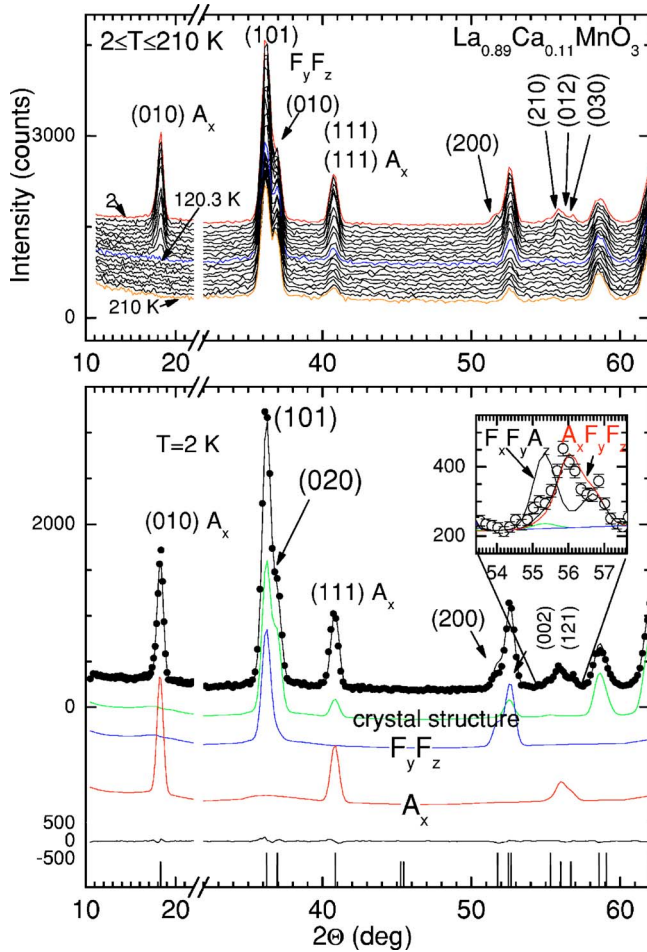
FIG. 12. (Color line) Upper panel: selected portion of the neutron powder-diffraction patterns for $La_{0.89}Ca_{0.11}MnO_3$ for $2 \leq T \leq 210$ K. Lower panel: decomposition of the neutron-diffraction pattern as $T=2$ K. Shown are the profiles coming from the A-antiferromagnetic, the ferromagnetic, and crystal structures. The inset shows the observed and calculated profiles for the Bragg peaks (210), (012), and (030) based on the models $F_xF_yA_z$ and $A_xF_yF_z$.

$La_{1-x}Sr_xMnO_3$ compound. The lattice parameters follow a monotonic temperature variation, contrary to ours. (c) The particular arrangement of the short bonds of Mn1-O and Mn2-O is different with that deduced from our data. Since no more data, from samples prepared with the method of Ref. 30, are available, we cannot safely further comment on the possible relation between the two studies.

It is interesting to discuss our crystal structure data in terms of the normal coordinates[7] of the octahedral complex MnO_6, Q_3, and Q_2. An arbitrary e_g orbital state can be written as $|\theta\rangle = \cos(\theta/2)|d_{z^2}\rangle + \sin(\theta/2)|d_{x^2-y^2}\rangle$. The orbitals $|d_{z^2}\rangle$ and $|d_{x^2-y^2}\rangle$ correspond to the states $|\theta=0\rangle$ and $|\theta=\pi\rangle$, respectively. It is also possible for the orbitals $(|d_{x^2}\rangle,|d_{y^2}\rangle)$ and $(|d_{z^2-x^2}\rangle,|d_{z^2-y^2}\rangle)$ to be formed. In this case we have $|\theta=\pm(2/3)\pi\rangle$ and $|\theta=\pm(1/3)\pi\rangle$, respectively. Experimentally the orbital filling can be estimated from crystallographic data, through the Mn-O bond lengths using the equation[7,8] $\tan\theta=Q_2/Q_3$, where $Q_3=2/\sqrt{6}(2m-l-s)$ and $Q_2=\sqrt{2}(l-s)$. Here l, m, and s mean long, medium, and short Mn-O bond lengths, respectively. The Q_2 mode mixes the $|d_{x^2-y^2}\rangle$ and

$|d_{z^2}\rangle$ orbitals and produces a two-sublattice orbital ordering pattern, with a lower energy orbital $\Psi_g=c_1|d_{x^2-y^2}\rangle\pm c_2|d_{z^2}\rangle$ and a higher energy orbital $\Psi_e=c_2|d_{x^2-y^2}\rangle\mp c_1|d_{z^2}\rangle$ ($\pm$ is referring to the two sublattices).

Using the crystallographic data at $T=300$ K of $LaMnO_3$ (Ref. 17) one finds $Q_3=-0.121$ Å and $Q_2=0.383$ Å. These values correspond to a canted antiferromagnetlike orbital arrangement with two sublattices, with $\theta=\pm72.38°$, respectively. Based on the crystallographic data of the present study we calculated the Q_2 and Q_3 parameters for the two cites predicted from $P2_1/c$ structural model. Figure 13 shows the temperature variation of Q_2 and Q_3 for the $x=0.125$, 0.15, and 0.175 samples. With solid lines we also plot the values which correspond to the $LaMnO_3$ compound. The first comment which can be made is that both Q_2 and $|Q_3|$ parameters for the two sites have lower values, in comparison to these of the $LaMnO_3$ compound. The second one is that both Mn sites have $Q_3\approx0$ with the first displaying a high value while the second a moderate one. Since we only have a small number of data it is difficult to recognize any change at $T_{M'/M''}$. The third comment is that only the sample $x=0.125$ shows non-monotonous variation of Q_2 at $T_{M'/M''}$. We note that for $T>T_{JT}$ the two sites pattern collapse into one site, with both Q_2 and Q_3 modes takng values near zero.

A. Comparison with the Sr compound

First of all, we must point out the similarities between the Sr and Ca based compounds, by comparing the neutron data from the stoichiometric $La_{1-x}Sr_xMnO_3$ $(0.1\leq x\leq0.2)$ of Dabrowski and co-workers[31,32] with ours. As Dabrowski *et al.* have pointed out,[31] the phase diagrams of the Sr case reported in the recent literature were constructed using physical and structural information obtained for dissimilar samples. Specifically, in the doping regime $0\leq x<0.3$ of the Sr compound the structure can form vacancies on both the $A(La,Sr)$ and $B(Mn)$ sites during synthesis under oxidizing conditions. Formation of an equal number of vacancies on the A and B sites would increase the average Mn oxidation state. Let us discuss our results with those of single-crystal data of the $La_{7/8}Sr_{1/8}MnO_3$ compound (this concentration is the most representative and widely studied of the particular regime) where very interesting results are available.

In a recent resonant x-ray scattering study on a $La_{7/8}Sr_{1/8}MnO_3$ single crystal, Geck *et al.*[33] have shown that the orbital state occurring in the interval $T_{MT}\leq T\leq T_{JT}$ (M means monoclinic and T triclinic) is similar to that found in $LaMnO_3$. For $T<T_{MT}$ an orbital reordering is compatible with the resonant data. This group[33] observed nonzero resonant and nonresonant intensity at $(3/2,3/2,3)$ superlattice reflection, only for $T<T_{MT}$. The nonresonant scattering in the particular reflection implies some kind of a superstructure modulation that develops at $T=T_{MT}$. Such behavior is related to structural and electronic degrees of freedom, speculatively attributed to the orbital polarons formation.[34,35] The work of Geck *et al.*[33] further supports the aspect that the CAF and FMI phases of Ca and Sr based $La_{1-x}(Ca,Sr)_xMnO_3$ compounds have both common characteristics and distinct differences. It seems that the vertical

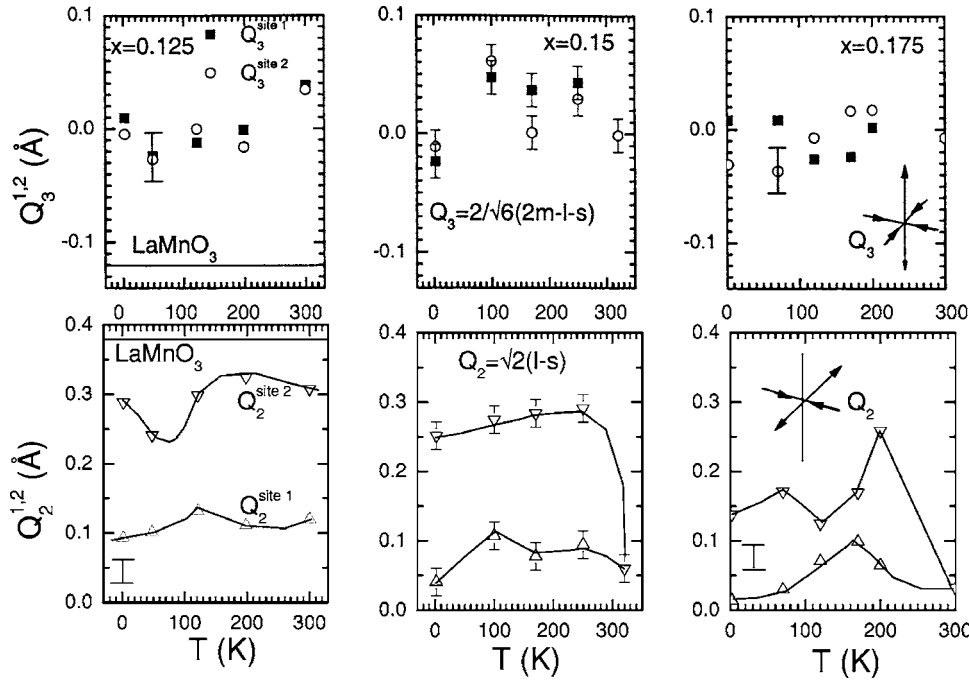FIG. 13. Temperature variation of the Q_2 and Q_3 parameters for $La_{1-x}Ca_x$ MnO_3 (x=0.125, 0.15, and 0.175) samples. The data for the $LaMnO_3$ compound are also included for a direct comparison (thin line).

boundary of the Sr case that separates the O^l CAF ground state from the triclinic new unknown orbital state exists even in the Ca case. Our results show that (a) similar to the Sr compound for $T_{MT} \lesssim T \lesssim T_{JT}$ the structure is monoclinic ($P2_1/c$); (b) based on our high-resolution synchrotron x-ray-diffraction data, the crystal structure of the Ca case remains monoclinic, while in the Sr case it is triclinic; and (c) both families of compounds exhibit significantly lower JT distortion in comparison with the M^l phase which occurs for $T_{M'M''} < T < T_{TJ}$.

B. Comparison between stoichiometric and cation deficient samples

We would like to emphasize once again that our results concern stoichiometric samples. The stoichiometric samples have properties different from those prepared in air.[9,36,37] The most prominent differences between the two families of samples are that the cation deficient samples do not display the CAF structure and do not undergo the characteristic co-operative JT distortion, irrespectively of the nominal calcium concentration. The second difference makes the cation deficient samples to be in an orbital liquid state below T_C, in the FMI regime, contrary to the stoichiometric ones where the ferromagnetic phase takes place in the cooperative ordered JT state at least in the interval $T_{M'M''} < T < T_C$. In addition, the cation deficient samples (e.g., x=0.1, 0.15 samples[36,38]) show an almost monotonous variation with temperature of the unit-cell parameters, satisfying also the inequality $c > a > b/\sqrt{2}$ (for $T < T_C$), contrary to the behavior observed in our stoichiometric samples where a pronounced nonmonotonous variation is observed. It is now well established that for low Ca concentrations the air prepared samples have cation vacancies.[9–11] The amount of vacancies increases as the nominal Ca concentration is near x=0. These samples are ferromagnetic irrespectively of x. The ordered magnetic mo-
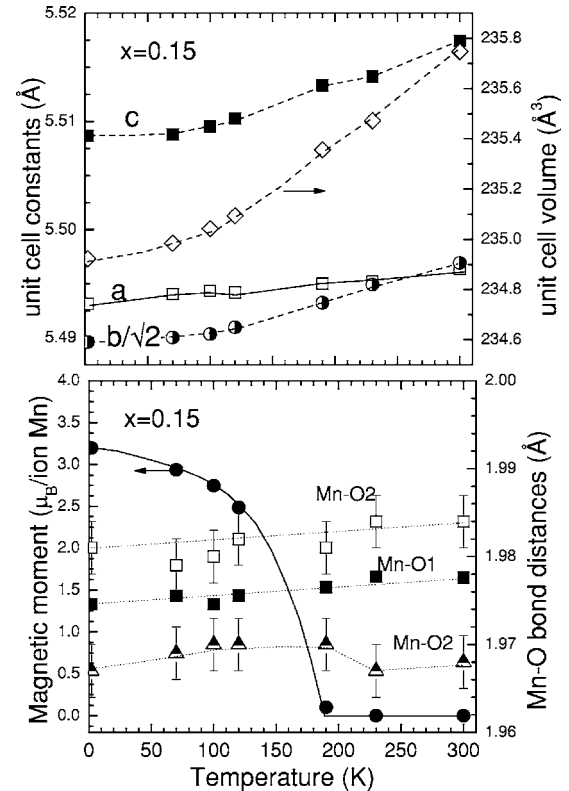

FIG. 14. Upper panel: temperature variation of the lattice parameters and unit-cell volume for $La_{0.85}Ca_{0.15}MnO_3$ compound prepared in air atmosphere. Lower panel: temperature variation of the ordered ferromagnetic moment and Mn-O$_i$ bond lengths. Lines through the experimental points are guides to the eye.

ment at zero temperature is significantly lower than the corresponding moment of the stoichiometric samples. For the $x=0.1$ and 0.15 nonstoichiometric samples the ordered magnetic moment was found $\sim 3\mu_B$ (Refs. 36, 38, and 39, while in our stoichiometric samples are obtained $\sim 3.7\mu_B$.

In order to check once more the situation we selected the $x=0.15$ sample, prepared in air for a detailed structural characterization using neutron-diffraction data. Figure 14 shows the temperature variation of the unit-cell parameters (upper panel), the ordered magnetic moment, and the Mn-O bond lengths (lower panel), as they were deduced from neutron-diffraction data using the E9 instrument. In perfect agreement with the above, this sample is a ferromagnetic insulator without the orthorhombic splitting that characterizes the cooperative JT distortion of the stoichiometric samples. Interestingly, the ordered magnetic moment is lower than the one of the reduced samples (e.g., $3.2\mu_B$ vs $3.7\mu_B$).

In the work of Algarabel *et al.*[39] that concerns a cation deficient sample with nominal $x=0.1$, significant small-angle neutron-scattering intensity (due to nanometric clusters) has been found to coexist with the long-range ferromagnetic phase. In our opinion, it is difficult to correlate these nanometric clusters with the anomalies observed for $T < T_{M/M//}$ in the stoichiometric samples because these clusters may be related with cation vacancies. It seems that in samples prepared in air the ratio $R(P_{O_2},T)=Mn^{+4}/Mn^{+3}$ is controlled by the partial oxygen pressure. When these samples are cooled slowly during the final preparation step the $R(P_{O_2},T)$ is different from the nominal Ca concentration, $R_x=x/(1-x)$. In order for the electric charge neutrality to be maintained, cation vacancies are created. This effect is significant for $x < 0.2$. Therefore in order to produce stoichiometric samples we must use reduced atmosphere conditions or quench the sample from high temperature to liquid N_2.[9–11] The presence of cation vacancies completely destroys the coherent JT distortion even for the $x=0$ sample.[9] In the cation deficient

samples first, it seems that the $R=Mn^{+4}/Mn^{+3}$ is locked to a nearly independent x value, and second, the $M^{/}$ phase which concerns a coherent JT distortion cannot be formed due to the cation vacancies. In this context numerous experiment results in the particular Ca regime should be interpreted. It is a mystery why the cation deficient samples show similar bulk magnetic measurements near $T=100$ K as the stoichiometric ones. The stoichiometric samples display a structural transition at $T_{M/M//}$ therefore it is reasonable to correlate this anomaly with the particular shape of the curves obtained in dc magnetic and ac susceptibility measurements. For nonstoichiometric samples such structural anomaly is absent leaving open the question about the relation of the bulk magnetization anomaly among the two families of samples.

Summarizing, the crystal structure refinements, from stoichiometric samples of the $La_{1-x}Ca_xMnO_3$ compound in the FMI regime, are presented. All the samples $(0.11 \leq x \leq 0.175)$ undergo a structural transition from O^* to $M^{/}$ structure at T_{JT}. High-resolution x-ray-diffraction data revealed that for $T < T_{JT}$, $La_{1-x}Ca_xMnO_3$ compounds $(0.11 \leq x \leq 0.175)$ have monoclinic $P2_1/c$ symmetry. The major structural characteristic of this model is the two Mn sites. As the bond lengths are concerned the Mn2 site displays properties similar with those of the Mn site of the $LaMnO_3$ compound, while the Mn1 site resembles the Mn site in the FMM regime. By further cooling, below the characteristic temperature $T_{M/M//}$, although, the structure remains the same, a strong reduction of the strain parameter $s=(a-c)/(a+c)$ is observed. This change has been accompanied by significant reduction of the monoclinic γ angle and is correlated with distinct changes in dc and ac magnetic measurements.

*Author to whom correspondence should be addressed. Email address: mpissas@ims.demokritos.gr

[1] D. Khomskii and G. Sawatzky, Solid State Commun. **102**, 87 (1997).

[2] L. Pinsard, J. Rodríquez-Carvajal, A. H. Moudden, A. Anane, A. Revcolevschi, and C. Dupas, Physica B **234-236**, 856 (1997).

[3] Y. Endoh, K. Hirota, S. Ishihara, S. Okamoto, Y. Murakami, A. Nishizawa, T. Fukuda, H. Kimura, H. Nojiri, K. Kaneko, and S. Maekawa, Phys. Rev. Lett. **82**, 4328 (1999).

[4] Y. Yamada, J. Suzuki, K. Oikawa, S. Katano, and J. A. Fernandez-Baca, Phys. Rev. B **62**, 11600 (2000).

[5] A. M. Glazer, Acta Crystallogr., Sect. B: Struct. Crystallogr. Cryst. Chem. **B28**, 3384 (1972); Acta Crystallogr., Sect. A: Cryst. Phys., Diffr., Theor. Gen. Crystallogr. **A31**, 756 (1975); C. J. Howard and H. T. Stokes, Acta Crystallogr., Sect. B: Struct. Sci. **B54**, 782 (1998); P. M. Woodward, *ibid.* **B53**, 32 (1997); **B53**, 44 (1997).

[6] As the present study reveals that the true structure below the T_{JT} is monoclinic, we prefer to keep the symbols $O^/$ and $O^{//}$ in order

to help the reader to compare our results with those of other studies.

[7] J. Kanamori, J. Appl. Phys. **31**, 14S (1960).

[8] K. I. Kugel' and D. I. Khomskii, Sov. Phys. Usp. **25**, 231 (1982).

[9] M. Pissas and G. Papavassiliou, J. Phys.: Condens. Matter **16**, 6527 (2004).

[10] B. Dabrowski, R. Dybzinski, Z. Bukowski, and O. Chmaissem, J. Solid State Chem. **146**, 448 (1999).

[11] J. A. M. van Roosmalen, E. H. P. Cordfuke, E. B. Helmholdt, and H. W. Zandbergen, J. Solid State Chem. **146**, 448 (1999).

[12] J. Rodríguez-Carvajal, Physica B **192**, 55 (1993).

[13] B. H. Toby, J. Appl. Crystallogr. **34**, 210 (2001).

[14] A. C. Larson and R. B. Von Dreele, General Structure Analysis System (GSAS), Los Alamos National Laboratory Report No. LAUR 86-748, 2000 (unpublished).

[15] L. W. Finger, D. E. Cox, and A. P. Jephcoat, J. Appl. Crystallogr. **27**, 892 (1994).

[16] G. Biotteau, M. Hennion, F. Moussa, J. Rodríguez-Carvajal, L. Pinsard, A. Revcolevschi, Y. M. Mukovskii, and D. Shulyatev,

Phys. Rev. B **64**, 104421 (2001).

[17] J. Rodríguez-Carvajal, M. Hennion, F. Moussa, A. H. Moudden, L. Pinsard, and A. Revcolevschi, Phys. Rev. B **57**, R3189 (1998).

[18] D. E. Cox, T. Iglesias, E. Moshopoulou, K. Hirota, K. Takahashi, and Y. Endoh, Phys. Rev. B **64**, 024431 (2001).

[19] P. W. Stephens, J. Appl. Crystallogr. **32**, 281 (1999).

[20] M. J. Calderon, A. J. Millis, and K. H. Ahn, Phys. Rev. B **68** 100401(R) (2003).

[21] K. H. Ahn, T. Lookman, and A. R. Bishop, Nature (London) **428**, 401 (2004).

[22] P. G. Radaelli, D. E. Cox, M. Marezio, and S.-W. Cheong, Phys. Rev. B **55**, 3015 (1997); P. G. Radaelli, G. Iannone, M. Marezio, H. Y. Hwang, S.-W. Cheong, J. D. Jorgensen, and D. N. Argyriou, *ibid.* **56**, 8265 (1997).

[23] J. Nogués, Vassil Skumryev, J. S. Muñoz, B. Martínez, J. Fontcuberta, L. Pinsard, and A. Revcolevschi, Phys. Rev. B **64**, 024434 (2001).

[24] H. Nojiri, K. Kaneko, M. Motokawa, K. Hirota, Y. Endoh, and K. Takahashi, Phys. Rev. B **60**, 4142 (1999).

[25] F. Moussa, M. Hennion, J. Rodríguez-Carvajal, H. Moudden, L. Pinsard, and A. Revcolevschi, Phys. Rev. B **54**, 15149 (1996); Q. Huang, A. Santoro, J. W. Lynn, R. W. Erwin, J. A. Borchers, J. L. Peng, and R. L. Greene, *ibid.* **55**, 14987 (1997).

[26] G. Shirane, Acta Crystallogr. **12**, 282 (1959).

[27] V. Markovich, E. Rozenberg, A. I. Shames, G. Gorodetsky, I. Fita, K. Suzuki, R. Puzniak, D. A. Shulyatev, and Ya. M. Mukovskii, Phys. Rev. B **65**, 144402 (2002).

[28] M. Pissas, G. Papavassiliou, E. Devlin, A. Simopoulos, and V. Likodimos, cond-mat/0403446.

[29] G. Papavassiliou, M. Pissas, M. Belesi, M. Fardis, J. Dolinsek, C. Dimitropoulos, and J. P. Ansermet, Phys. Rev. Lett. **91**, 147205 (2003).

[30] M. V. Lobanov, A. M. Balagurov, V. Ju. Pomjakushin, P. Fischer, M. Gutmann, A. M. Abakumov, O. G. Dyachenko, E. V. Antipov, O. I. Lebedev, and G. Van Tendeloo, Phys. Rev. B **61**, 8941 (2000).

[31] B. Dabrowski, X. Xiong, Z. Bukowski, R. Dybzinski, P. W. Klamut, J. E. Siewenie, O. Chmaissem, J. Shaffer, C. W. Kimball, J. D. Jorgensen, and S. Short, Phys. Rev. B **60**, 7006 (1999).

[32] X. Xiong, B. Dabrowski, O. Chmaissem, Z. Bukowski, S. Kolesnik, R. Dybzinski, C. W. Kimball, and J. D. Jorgensen, Phys. Rev. B **60**, 10186 (1999).

[33] J. Geck, P. Wochner, D. Bruns, B. Büchner, U. Gebhardt, S. Kiele, P. Reutler, and A. Revcolevschi, Phys. Rev. B **69**, 104413 (2003).

[34] T. Mizokawa, D. I. Khomskii, and G. A. Sawatzky, Phys. Rev. B **61**, R3776 (2000).

[35] R. Kilian and G. Khaliullin, Phys. Rev. B **58**, R11841 (1998).

[36] Q. Huang, A. Santoro, J. W. Lynn, R. W. Erwin, J. A. Borchers, J. L. Peng, K. Ghosh, and R. L. Greene, Phys. Rev. B **58**, 2684 (1998); Q. Huang, A. Santoro, J. W. Lynn, R. W. Erwin, J. A. Borchers, J. L. Peng, and R. L. Greene, *ibid.* **55**, 14987 (1998); J. W. Lynn, R. W. Erwin, J. A. Borchers, Q. Huang, A. Santoro, J.-L. Peng, and Z. Y. Li, Phys. Rev. Lett. **76**, 4046 (1996).

[37] P. Dai, J. Zhang, H. A. Mook, S.-H. Liou, P. A. Dowben, and E. W. Plummer, Phys. Rev. B **54**, R3694 (1996).

[38] P. Dai, J. Zhang, H. A. Mook, F. Foong, S.-H. Liou, P. A. Dowben, and E. W. Plummer, Solid State Commun. **100**, 865 (1996).

[39] P. A. Algarabel, J. M. De Teresa, J. Blasco, M. R. Ibarra, Cz. Kapusta, M. Sikora, D. Zajac, P. C. Riedi, and C. Ritter, Phys. Rev. B **67**, 134402 (2003).